

Article

3d (Co and Mn) and 4d (Ag) Transition Metal-Doped ZnO Nanoparticles Anchored on CdZnS for the Photodegradation of Rhodamine B

Ann Wangari Mureithi ¹, Chen Song ¹, Thi Kim Tran Tran ¹, Hawi N. Nyiera ¹, Xueni Huang ¹, Tejas S. Bhosale ¹, Abiodun Daniel Aderibigbe ^{1,2}, Ranjana Burman ¹, Steven L. Suib ^{1,2} and Jing Zhao ^{1,2,*} 

¹ Department of Chemistry, University of Connecticut, 55 North Eagleville Rd., Storrs, CT 06269-3060, USA; xueni.huang@uconn.edu (X.H.); ranjana.burman@uconn.edu (R.B.)

² Institute of Materials Science, University of Connecticut, 97 North Eagleville Rd., Storrs, CT 06269-3137, USA

* Correspondence: jing.zhao@uconn.edu

Abstract: The construction of a heterojunction by coupling two semiconductor photocatalysts with appropriate band positions can effectively reduce the recombination of photogenerated charge carriers, thus improving their catalytic efficiency. Recently, ZnO photocatalysts have been highly sought after in the synthesis of semiconductor heterostructures due to their wide band gap and low conduction band position. Particularly, transition metal-doped ZnO nanoparticles are attractive due to the additional charge separation caused by temporary electron trapping by the dopant ions as well as the improved absorption of visible light. In this paper, we compare the effect of doping ZnO nanoparticles with 3d (Co and Mn) and 4d (Ag) transition metals on the structural and optical properties of ZnO/CdZnS heterostructures and their photocatalytic performance. With the help of scanning electron microscopy, the successful anchoring of doped and undoped ZnO nanoparticles onto CdZnS nanostructures was confirmed. Among the different heterostructures, Ag-doped ZnO/CdZnS exhibited the best visible-light-driven degradation of rhodamine B at a rate of $1.0 \times 10^{-2} \text{ min}^{-1}$. The photocurrent density analysis showed that AgZnO/CdZnS has the highest amount of photogenerated charges, leading to the highest photocatalytic performance. The reduction in the photocatalytic performance in the presence of hole scavengers and hydroxyl radical scavengers confirmed that the availability of photogenerated electrons and holes plays a pivotal role in the degradation of rhodamine B.

Keywords: semiconductor heterostructures; transition metal-doped ZnO; CdZnS; charge separation; photocatalysis



Citation: Mureithi, A.W.; Song, C.; Tran, T.K.T.; Nyiera, H.N.; Huang, X.; Bhosale, T.S.; Aderibigbe, A.D.; Burman, R.; Suib, S.L.; Zhao, J. 3d (Co and Mn) and 4d (Ag) Transition Metal-Doped ZnO Nanoparticles Anchored on CdZnS for the Photodegradation of Rhodamine B. *Crystals* **2024**, *14*, 41. <https://doi.org/10.3390/cryst14010041>

Academic Editors: Kai Yu, Yue Chang and Minmin Han

Received: 12 December 2023

Revised: 24 December 2023

Accepted: 26 December 2023

Published: 28 December 2023



Copyright: © 2023 by the authors. Licensee MDPI, Basel, Switzerland. This article is an open access article distributed under the terms and conditions of the Creative Commons Attribution (CC BY) license (<https://creativecommons.org/licenses/by/4.0/>).

1. Introduction

Constructing a heterojunction between two semiconductors is one of the most desired ways to obtain efficient photocatalysts [1]. Heterojunctions are formed when two semiconductors that possess different energy band structures are brought into contact, resulting in an electric field at the interface due to the spontaneous diffusion of electrons between the semiconductors [2–4]. As a result, semiconductor heterostructures in photocatalysis can facilitate the separation of photogenerated electrons and holes and improve their redox abilities [5,6]. Different types of heterojunctions have been achieved, categorized depending on the band alignment between the constituent semiconductors. Among them, Z-type heterojunctions exhibit significant charge separation upon photoexcitation [7–9]. This type of heterojunction is formed when both the valence band (VB) and conduction band (CB) positions of the semiconductor with a higher Fermi level (E_f) are higher than those of the semiconductor with a lower E_f [10–12]. When photoexcited, electrons in the semiconductor with a lower E_f could travel across the interface and reduce the holes in the semiconductor

with the higher E_f ; therefore, the electrons in the semiconductors with a high E_f and holes in the semiconductors with a low E_f are available for redox reactions [13,14].

Some of the widely explored Z-type heterojunctions are ZnO-based heterostructures. When used solely, ZnO nanomaterials exhibit an impressive photocatalytic performance in photoreactions, such as water splitting for H_2 production and the decomposition of organic pollutants [15–19]. Additionally, the high oxidation potential of ZnO's VB edge (~ 3.0 eV vs. NHE, normal hydrogen electrode) allows the photoinduced holes to effectively oxidize a wide range of molecules, including water [20]. However, like many powder semiconductor photocatalysts, there are some drawbacks in their applications, such as leaching, aggregation, and agglomeration in the reaction solution upon excitation by light [21]. This leads to deterioration in the performance as well as the release of toxic constituent elements [22]. In addition, unfavorable sunlight absorption is limited to the UV region (only $\sim 5\%$ of the solar energy) due to the wide band gap (3.37 eV) and fast electron–hole recombination [23–25]. The formation of a Z-type heterostructure using ZnO and a narrow band gap semiconductor is a plausible remedial strategy to reduce charge recombination within ZnO. One such heterojunction consists of ZnO/CdZnS [23]. When ZnO/CdZnS heterostructures are irradiated, the electrons in the CB of CdZnS (higher E_f) and the holes in the VB of ZnO (lower E_f) can be utilized in photo-redox reactions.

Another strategy for the suppression of charge recombination is the incorporation of dopant ions in ZnO [26–29]. The addition of dopant ions creates localized energy states within the band gap and reduces charge recombination as well as narrowing the band gap of ZnO, which increases visible light absorption [30–33]. First-row transition metals are the commonly used dopants in ZnO nanoparticles due to their similarities in properties, such as ionic radii [34–36]. However, transition metals in other periods (4d and 5d), such as the noble metals Au, Ag, and Pd as well as Cd, have also been successfully applied as dopants in ZnO nanoparticles to improve ZnO catalytic performance [37–40]. The differences between 3d transition metals and transition metals in higher periods, such as ionic radii and oxidation potentials, could impact ZnO structural and optical properties and photocatalytic performance differently. A clear understanding is lacking of how transition metal dopants in different periods (for example, 3d and 4d) affect the properties of ZnO and the subsequent photocatalytic efficiency of ZnO-based heterostructures. This work compares the impact of 3d (Co, Mn) and 4d (Ag) transition metal dopants in ZnO nanoparticles on the photocatalytic properties of ZnO/CdZnS-based heterostructures. It was observed that Ag-doped ZnO/CdZnS showed higher photocatalytic activity in rhodamine B degradation than Co- and Mn-doped ZnO/CdZnS heterostructures. Reduced charge recombination within AgZnO was found to be a key factor that improves the photocatalytic activity of AgZnO/CdZnS.

2. Experimental Section

2.1. Chemicals

All chemicals were purchased from Sigma Aldrich, Burlington, MA USA, and were used as received without further purification: cadmium chloride ($CdCl_2$, 99.99%, trace metal basis), zinc acetate dihydrate ($Zn(CH_3CO_2)_2 \cdot 2H_2O$, $\geq 98\%$), thioacetamide (C_2H_5NS , $\geq 99.0\%$), lysine ($C_6H_{14}N_2O_2$), $\geq 98\%$, TLC), methanol, acetone, potassium hydroxide (KOH, $\geq 85\%$, pellets), silver nitrate ($AgNO_3$, $\geq 99.0\%$), manganese (II) acetate tetrahydrate ($Mn(CH_3CO_2)_2 \cdot 4H_2O$, $\geq 99\%$), cobalt (II) acetate tetrahydrate ($Co(CH_3CO_2)_2 \cdot 4H_2O$, $\geq 98.0\%$), and rhodamine B ($C_{28}H_{31}ClN_2O_3$), $\geq 95\%$, HPLC).

2.2. Synthesis of CdZnS Nanostructures

A total of 1.28 g of cadmium chloride, 0.658 g of zinc acetate dihydrate, 360 mg of thioacetamide, and 20 mg of lysine were added to 100 mL of deionized water in a 250 mL round-bottomed flask. The mixture was heated for 2 h at $100^\circ C$ under constant stirring. A yellow precipitate formed was isolated by centrifugation at 3500 rpm and was washed several times with water.

2.3. Synthesis of Undoped and Doped ZnO Nanoparticles

A total of 4.38 g of zinc acetate dihydrate in 15 mL of methanol was heated to 60 °C while stirring for 30 min. A 5 mL solution of 1.1 g of potassium hydroxide in 5 mL of methanol was then added dropwise and left at the same temperature for 2 h. The white precipitate was collected via centrifugation and washed using methanol. Afterward, the product was dried and heated at 150 °C in a vacuum oven for 2 h.

Ag-, Mn-, and Co-doped ZnO nanoparticles were prepared following the same procedure, except that the 2.5% molar ratio of the corresponding precursor (silver nitrate, manganese (II) acetate tetrahydrate, or cobalt (II) acetate tetrahydrate) was also added to the zinc acetate dihydrate solution before heating.

2.4. Synthesis of ZnO-CdZnS and Doped ZnO-CdZnS Heterostructures

To fabricate ZnO/CdZnS, 0.219 g of zinc acetate dihydrate in 15 mL of methanol was first heated to 60 °C while stirring for 30 min. A total of 200 mg of the synthesized CdZnS nanostructures was then added to the solution. Immediately after this, 0.055 g of potassium hydroxide in 5 mL of methanol was added dropwise and left at the same temperature for 2 h. Doped ZnO/CdZnS heterostructures were synthesized following the same procedure as that of ZnO/CdZnS, except that a 2.5% molar ratio of the dopant precursor was added to the zinc acetate dihydrate in the first step of the reaction.

2.5. Photocatalytic Degradation of Rhodamine B

The solutions for photocatalytic reactions consisted of 4 mg/L of rhodamine B and 1 mg/mL of the photocatalyst dispersed in water with a final volume of 3 mL in a quartz cuvette. The sample solutions were first left to stir in the dark for 45 min to obtain the adsorption–desorption equilibrium. A broadband (360 to 900 nm) LED lamp with an output power of 30 mW was used to irradiate the samples. At specified reaction times, the extent of the photodegradation was analyzed. The sample solutions were centrifuged at 3000 rpm for 2 min to remove the photocatalyst, to avoid errors in the UV-vis absorption spectra of rhodamine B resulting from light scattered by the photocatalysts. The precipitate was set aside, and the supernatant was analyzed via UV-vis spectroscopy. After each analysis, the photocatalysts were redispersed in the sample solution and left under illumination for further reaction.

2.6. Photocatalytic Trapping Experiment

Ethanol and isopropanol were used as hole and hydroxyl radical scavengers, respectively. A total of 4 mg/L of rhodamine B and 1 mg/mL of the AgZnO/CdZnS photocatalysts were dispersed in 3 mL of ethanol or isopropanol. The samples were stirred in the dark for 45 min and subsequently illuminated for 75 min by the same light source used for the photocatalytic degradation. Before the UV-vis analysis of the sample, the photocatalyst was removed by centrifugation at 3000 rpm for 2 min.

2.7. Instrumentation

Powder X-ray diffraction patterns were obtained using a Rigaku ultima IV powder X-ray diffractometer by Rigaku, Wilmington, MA USA, with Cu K α (1.54 Å) radiation and operated at 40 kV and 44 mA [41]. TEM images were taken using a Talos F200X from Thermo Fisher Scientific, Waltham, MA, USA, that has an accelerating voltage of 200 kV. The morphology of the synthesized materials was investigated using a Verios 460 L SEM manufactured by Thermo Fisher Scientific, Waltham, MA USA. UV-vis spectra were acquired using an Agilent technologies Cary—60 UV-vis spectrometer made by Agilent, Santa Clara, CA USA. PL spectra were attained using a Horiba FluoroMax spectrofluorometer manufactured by Horiba, Piscataway, NJ USA. The comparison of the oxygen vacancies in the undoped and doped ZnO nanoparticles was achieved on a Thermo Fischer Scientific, Waltham, MA USA, X-ray photoelectron spectrometer (Model: K-Alpha, part number: 1200505) with an Al(mono) X-ray source (1486.6 eV). Peak fittings were conducted using

CasaXPS (Casa Software Limited, Teignmouth, United Kingdom) and charge correction was performed concerning the C 1 s photoelectron line (284.8 eV). Photocurrent measurements were performed in a testing cell arranged with a 3-electrode system composed of SCE as the reference electrode, platinum counter electrode, and ITO coated-glass electrodes as the working electrode in a 0.1 M Na₂SO₄ electrolyte solution. The illuminating light source was a UV-vis full-range light with a power of 300 W, purchased from Newport Corporation, Franklin, MA USA.

3. Results and Discussion

The synthesized nanomaterials' crystal structures and crystallite sizes were determined using powder XRD; the results are shown in Figure 1a. The XRD patterns for the CdZnS nanostructures matched those of hexagonal CdS. No peaks associated with the hexagonal crystal phase of ZnS were registered because, at a molar ratio of 70:30 Cd:Zn, the predominant features of CdZnS are expected to resemble those of CdS. The analysis of the heterostructures showed the simple combination of the diffraction peaks from the undoped and doped ZnO nanoparticles and CdZnS nanostructures, confirming that the crystal structure of CdZnS was not altered during the anchoring of the doped and undoped ZnO nanoparticles onto the CdZnS nanostructures.

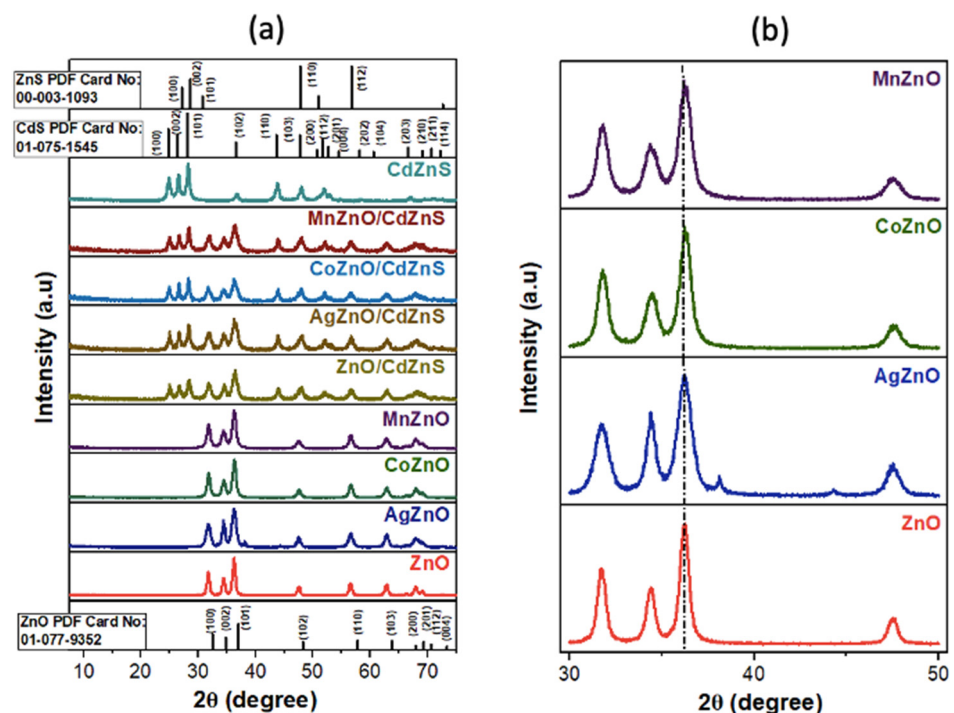


Figure 1. XRD patterns for (a) the doped and undoped ZnO nanoparticles and the doped and undoped ZnO and CdZnS heterostructures. (b) Magnified XRD patterns for the doped and undoped ZnO nanoparticles.

From a closer look at the diffraction patterns for the undoped ZnO nanoparticles in Figure 1b, they exhibited peaks at 2θ degrees that were indexed to the hkl crystal planes of the hexagonal wurtzite crystal phase of ZnO [42]. These same diffraction patterns were recorded in the Co- and Mn-doped ZnO nanoparticles. The absence of foreign peaks for the oxides of cobalt and manganese indicated that the addition of a dopant did not alter the crystal structure of ZnO [43]. However, two additional small peaks at 38 and 44 degrees were seen in the XRD pattern of AgZnO, which correspond to the Ag(111) and Ag(200) planes [44], respectively, likely because some Ag⁺ was reduced to Ag⁰ and subsequently nucleated to form Ag domains. Peak broadening, often seen upon successful doping, was observed in the doped ZnO nanoparticles [45]. The magnified diffraction

patterns in Figure 1b clearly showed that, among Co-, Mn-, and Ag-doped ZnO, the AgZnO nanoparticles displayed the most peak broadening. The broadening of the diffraction peaks indicates a reduction in the crystalline size of ZnO upon substituting Zn^{2+} with Co^{2+} , Mn^{2+} , and Ag^+ [46]. The larger size of the 4d metal cation Ag^+ (115 pm) compared to those of the 3d metal cations Co^{2+} (74 pm) and Mn^{2+} (83 pm) may have impaired the incorporation of Ag^+ into the Zn^{2+} (74 pm) site in the crystal, resulting in the lattice distortion of the ZnO nanoparticles. In addition, the crystallite size calculations obtained using Scherrer's equation and noted in Table S1 revealed that AgZnO had the smallest crystallite size of 3.4 nm compared to 7.3 nm, 5.6 nm, and 5.1 nm for ZnO, CoZnO, and MnZnO respectively. This is because, among all the doped ZnO nanoparticles, AgZnO could have more stress induced in the crystal edges and boundaries during the growth and formation process due to the presence of a large Ag^+ cation [20,47].

The morphology of the undoped and doped ZnO nanoparticles and the CdZnS-based heterostructures was revealed by TEM and SEM. The TEM micrographs of the undoped and doped ZnO are displayed in Figure 2. The morphology of the ZnO nanoparticles was quasi-spherical structures. Similar morphologies were observed for the Ag-, Co-, and Mn-doped ZnO nanoparticles. However, diameter size calculation obtained using ImageJ software revealed a decrease upon doping from 21 ± 4 nm for ZnO to 13 ± 4 nm, 15 ± 2 nm, and 17 ± 3 nm for AgZnO, CoZnO, and MnZnO, respectively. The SEM images of the CdZnS nanostructures and the undoped and doped ZnO/CdZnS heterostructures are shown in Figure 3a–e. The CdZnS nanostructures appeared aggregated due to the heating process in the synthesis. In each micrograph of the heterostructures, many lighter dots appeared on the CdZnS nanostructures, resulting from the undoped or doped ZnO nanoparticles. These images demonstrated the successful growth of the undoped and doped ZnO nanoparticles on CdZnS.

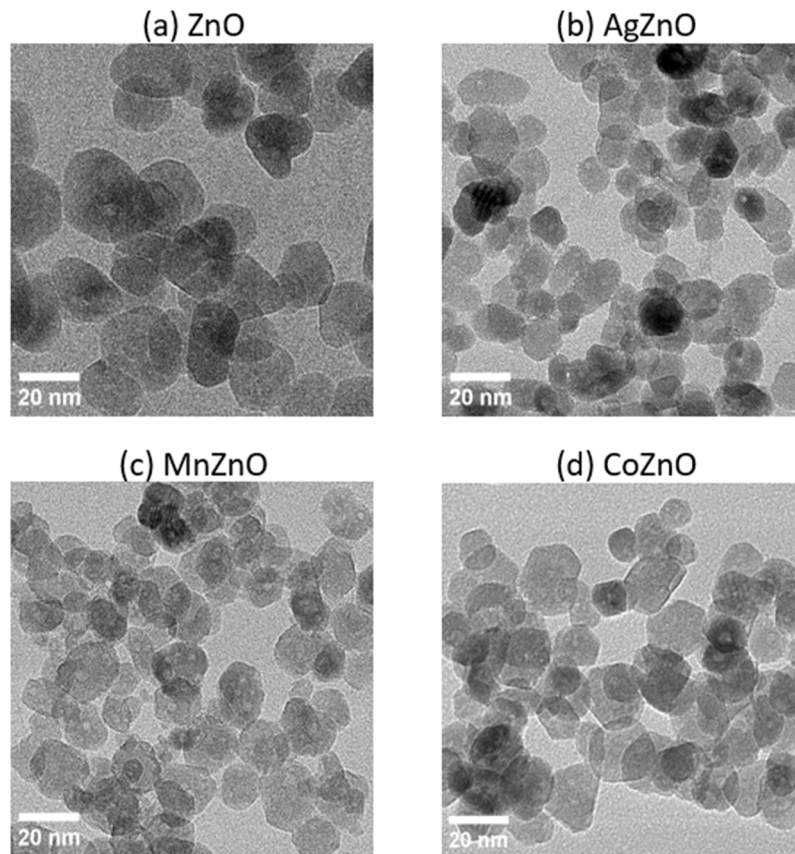


Figure 2. (a–d) TEM images for the undoped and doped ZnO nanoparticles. Scale bars = 20 nm.

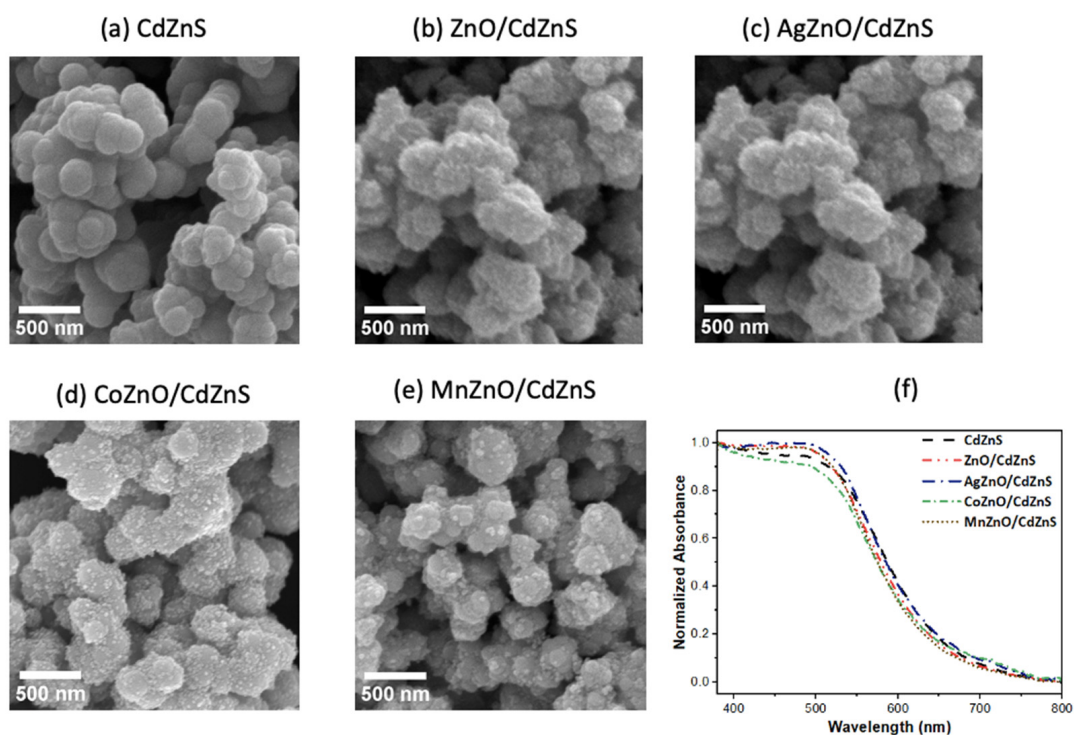


Figure 3. (a–e) SEM images of CdZnS and the undoped and doped ZnO/CdZnS heterostructures. Scale bars = 500 nm. (f) Diffuse reflectance UV-vis spectra of CdZnS, ZnO/CdZnS, and the doped ZnO/CdZnS heterostructures.

The optical features of the undoped and doped ZnO/CdZnS heterostructures were determined by UV-vis diffuse reflectance spectroscopy (DRS). The samples were prepared by evenly spreading 20 mg of each sample on 1 g of barium sulfate standard powder. The obtained UV-vis diffuse reflectance spectra in Figure 3f showed negligible shifts in the absorption edges of the undoped and doped ZnO/CdZnS heterostructures from that of CdZnS. The DRS absorption peaks of ZnO and the Ag-, Co-, and Mn-doped ZnO nanoparticles are shown in Figure S1a. These features were not observed in the DRS spectra due to the low amounts of nanoparticles (10% by weight) in the heterostructures.

The visible-light-driven photocatalytic performance of the heterostructures was evaluated by comparing the rate and extent of rhodamine B dye photodegradation. Rhodamine B is a common synthetic dye used mainly in textile industries, which, upon release to the environment in wastewater, poses health risks to both humans and animals [48]. Its effective removal from wastewater is thus important. In this work, rhodamine B was particularly adequate for photocatalytic performance testing because its UV-vis absorption at 55 nm did not overlap with the absorbance of the photocatalysts used. The change in rhodamine B concentration in the samples upon irradiation was monitored by analyzing the UV-vis absorbance. Figures 4a and S2 show the UV-vis spectra of rhodamine B at varying reaction times using the different photocatalysts. The adsorption–desorption equilibrium was achieved between –45 min (45 min before visible light illumination) and 0 min. The decrease in dye concentration in the solution was due to the dye’s adsorption on the surface of the photocatalyst [49]. With the increase in the irradiation time, the absorbance of rhodamine 6G decreased. Among the photocatalysts tested, AgZnO/CdZnS showed the highest photocatalytic performance, exhibiting 88% photodegradation after 100 min of illumination with visible light.

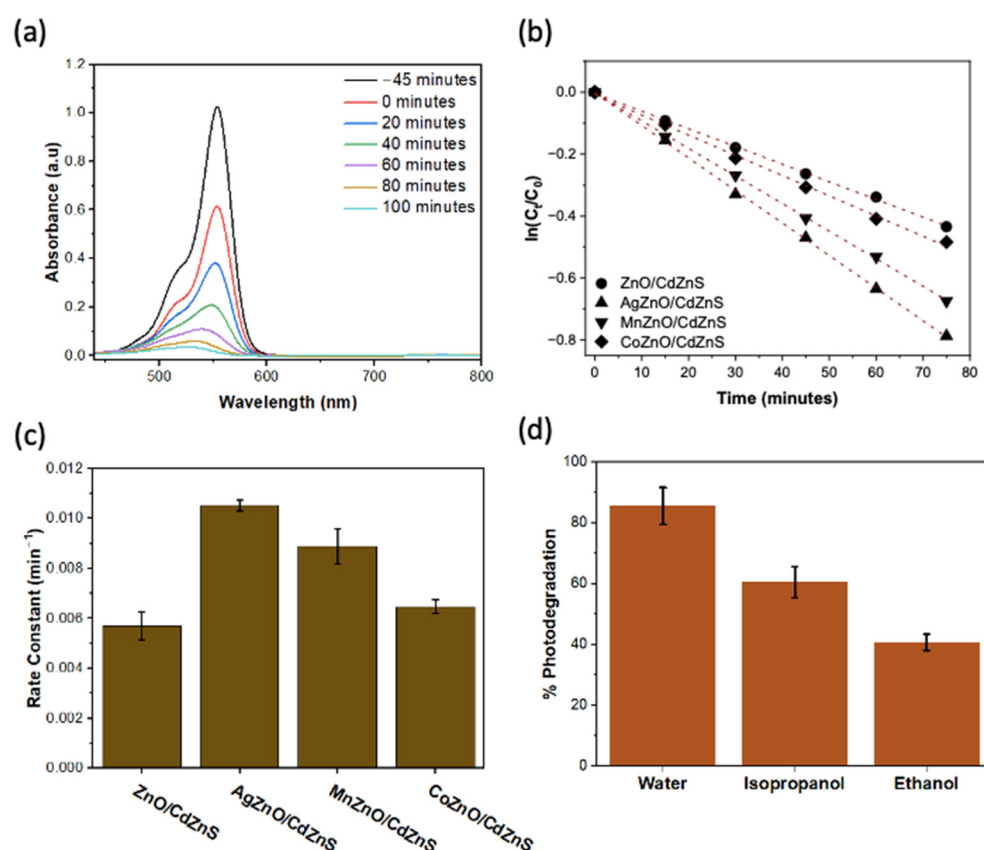
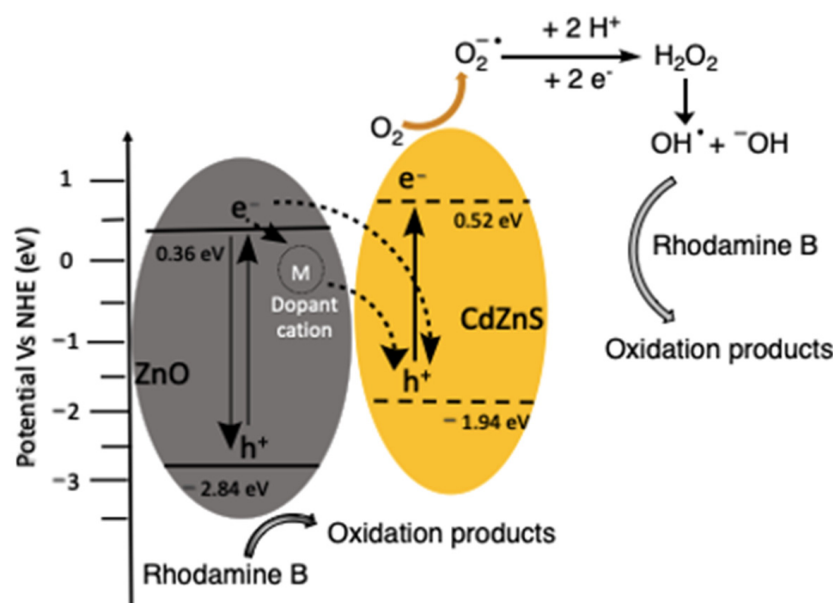


Figure 4. (a) UV-vis spectra of rhodamine B during photodegradation reaction using AgZnO/CdZnS at specified time intervals. (b) Kinetic study of the time-dependent degradation of 4 mg/L of a rhodamine B solution using 1 mg/mL of the photocatalyst under visible light irradiation. (c) Bar graph representation of the rate constants for the reaction using different photocatalysts. (d) Scavenging experiment comparing the photodegradation of rhodamine B in water and in two scavengers. In both (c,d), 3 experimental trials were carried out for each material. The representative bar graphs are the average values, and the error bars are representative of the standard deviations.

The rhodamine B degradation reaction was recognized to follow first-order kinetics [50]. The results are presented in Figure 4b as linear plots of $\ln(C/C_0)$ versus time, where C is the concentration of rhodamine B after a specified irradiation time and C_0 is the initial concentration of the dye [50]. Among all the doped ZnO/CdZnS heterostructures, AgZnO/CdZnS exhibited the best photocatalytic performance, at a rate of $1.0 \times 10^{-2} \text{ min}^{-1}$, which is 1.2 and 1.6 times faster than those of MnZnO/CdZnS and CoZnO/CdZnS, respectively. This high performance of AgZnO/CdZnS is comparable to those of N-TiO₂/rGO nanocomposites and g-C₃N₄ nanorods, which were recently reported to degrade 78% Rhodamine B in 90 minutes, or at a rate of $1 \times 10^{-2} \text{ min}^{-1}$, respectively [51,52]. The proposed mechanism for the degradation process using the heterostructures is illustrated in Scheme 1. Upon illumination, photoexcited electrons and holes are generated in the VB and CB of the two constituent semiconductors, respectively. The excitons could directly recombine within each semiconductor (not shown in the scheme). Alternatively, electrons in the CB of the doped ZnO could directly recombine with the holes in the VB of CdZnS as in a Z-scheme system, or they could temporarily transfer to the dopant Ag⁺, Co²⁺, or Mn²⁺ cations. These cations act as electron traps for a short duration. Next, the trapped electrons in the doped ZnO are released to reduce the holes in CdZnS or to directly react with the O₂ adsorbed on the catalysts. The electrons in the CB of CdZnS reduce O₂ to O₂^{-•}, which are then reduced to form the OH[•] radical. Subsequently, OH[•] oxidizes rhodamine B to obtain degradation products and H₂O. The holes in AgZnO, CoZnO, and MnZnO could also oxidize the rhodamine B dye to yield degradation products.



Scheme 1. Proposed photocatalytic mechanism for the degradation of rhodamine B using transition metal-doped ZnO anchored on CdZnS.

To confirm the role of holes (h^+) and OH^\bullet in the reaction, scavenging experiments were conducted using a hole scavenger (ethanol) and a hydroxy radical (isopropanol). Experimentally, AgZnO/CdZnS were dispersed in either ethanol or isopropanol for the reactions instead of water. Figure 4d shows an obvious decrease in the photodegradation of rhodamine B by 52.3% in the presence of hole scavengers (ethanol) and 29.3% when hydroxy radical scavengers (isopropanol) are present. The decrease in the photocatalytic degradation when both holes and OH^\bullet are removed revealed that the photogenerated holes and OH^\bullet obtained from the photogenerated electrons were critical for the successful degradation reaction using AgZnO/CdZnS.

We hypothesize that the major reason causing the higher photocatalytic efficiency of AgZnO/CdZnS, compared to those of CoZnO/CdZnS and MnZnO/CdZnS, is due to the greater suppression of charge recombination in the presence of Ag^+ than of Co^{2+} and Mn^{2+} . To verify this, charge carrier density measurements were carried out by testing the hydrogen evolution reaction (HER) using the undoped and doped ZnO/CdZnS under dark and light conditions. The results are displayed in Figure 5b. The dark and light current densities represent the electrochemical and photoelectrochemical performances of the samples applied in the HER reaction, respectively. The difference between the light and dark current density, referred to as ΔJ , represents the density of the charge carriers generated from light. As observed in the results, AgZnO/CdZnS showed the highest ΔJ ($2.82 \mu A \cdot cm^{-1}$) and, therefore, the highest charge carrier density among all the tested heterostructures. The high charge carrier density represents a way to confirm the optimal charge separation in AgZnO/CdZnS [53,54].

One possible reason for the better charge separation in AgZnO/CdZnS than in the other heterostructures is the higher oxidizing power of Ag^+ compared to those of Co^{2+} and Mn^{2+} . Hence, Ag^+ has a greater ability to temporarily accept photoexcited electrons from the VB of ZnO. The electrons from Ag are subsequently released to reduce the holes in the VB of CdZnS. This process reduces exciton recombination in both ZnO and CdZnS. Other than the largest enhancement in charge separation by Ag doping, a few other factors should be considered. Firstly, pure Ag domains were detected in the Ag-doped ZnO nanoparticles according to the XRD spectrum in Figure 1b, as well as the AgZnO XPS spectrum (as displayed in Figure S3a) that shows Ag 3d peaks arise from metallic Ag. These observations suggest that the Ag/CdZnS metal-semiconductor heterojunction could have subsequently formed and facilitated the charge separation [55,56]. Additionally, both

the AgZnO and CoZnO nanoparticles were found to have slightly narrower band gaps than those of MnZnO and ZnO. Consequently, AgZnO/CdZnS and CoZnO/CdZnS could have slightly increased the light absorption during photoexcitation, thus improving the photocatalytic performance [57,58]. Lastly, XPS studies have revealed that doping has impact on the amount of oxygen vacancies in ZnO. By deconvolution of the O 1s spectrum using Gaussian functions, 3 peaks corresponding to lattice oxygen, adsorbed oxygen, and oxygen vacancies were obtained as is shown in Figure S3b. A comparison of the percent oxygen vacancies as is given in Table S2 reveals that the incorporation of Ag⁺ dopants increased the oxygen vacancies in the heterostructures compared to ZnO alone. The increase could be beneficial to the photocatalyst. Upon photoexcitation, these oxygen vacancies could temporarily trap electrons that could then be released and used in the photocatalytic reaction, thus contributing to enhanced charge separation [59]. Considering all these factors, the highest photocatalytic efficiency of the AgZnO/CdZnS heterostructures was achieved among all the catalysts tested.

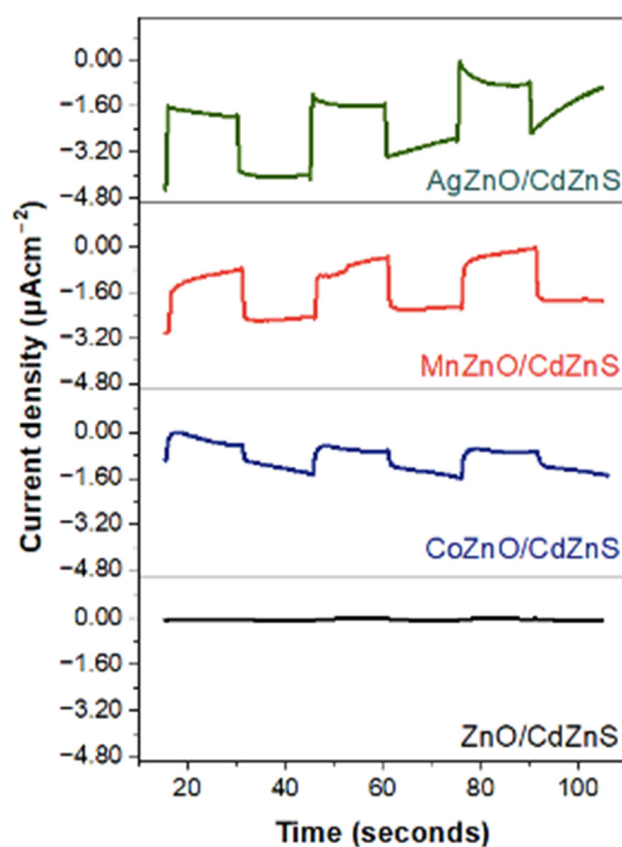


Figure 5. Photocurrent density–time curves for the different heterostructures.

4. Conclusions

In this work, we reported the impact of doping ZnO nanoparticles with 3d (Co and Mn) and 4d (Ag) transition metals on the photocatalytic performance of ZnO/CdZnS heterostructures. The photodegradation of rhodamine B conducted by illumination with visible light showed that AgZnO/CdZnS achieved a better photocatalytic activity than CoZnO/CdZnS and MnZnO/CdZnS. The photocurrent density study revealed that this good performance was hinged upon the effective charge separation in AgZnO/CdZnS, which is possibly a result of the higher oxidizing power of Ag⁺ compared to those of Co²⁺ and Mn²⁺. Additionally, the XRD data showed that, when Ag⁺ was the dopant transition metal, Ag domains were formed, which also facilitated the charge separation via the formation of metal/semiconductor heterostructures. This work showed that, although it is more plausible to substitute Zn²⁺ in ZnO with a transition metal dopant in the 3d

period due to similarities in atomic properties compared to metals in different periods, the photocatalytic performance of heterostructures based on the 3d transition metal-doped ZnO is not necessarily better. The impact of the dopant cation on the structural and optical properties of ZnO as well as its contribution to charge separation is vital. Hence, there is a need to explore further the performance of heterostructures based on not only 3d transition metal-doped ZnO but also 4d and 5d transition metal-doped ZnO.

Supplementary Materials: The following supporting information can be downloaded at: <https://www.mdpi.com/article/10.3390/cryst14010041/s1>. Included in the Supplementary Materials are the crystallite sizes, band gap determination, and XPS results and data analysis for the undoped and Ag-, Co-, and Mn-doped ZnO, and UV-vis spectra for the degradation of rhodamine B using different photocatalysts. Figure S1: (a) Diffuse reflectance UV-vis spectra of ZnO and Ag, Co, and Mn doped ZnO nanoparticles. (b) to (e) are the band gap determination plot of $(F(R)h\nu)^n$ vs $h\nu$ obtained from diffuse reflectance data; Figure S2: (a–e) UV-vis spectra for the degradation of Rhodamine B using different photocatalysts; Figure S3: (a) XPS spectra for O 1s, Zn 2p, Mn 2p, Zn 3s and Zn 3d and Ag 3d. (b) Enlarged XPS spectra of O1s peaks and deconvolutions representing the binding energies of the lattice oxygen (OL), chemisorbed oxygen (Oads), and oxygen vacancies (OV); Table S1: Calculated crystallite sizes of ZnO and Ag, Mn, and Co-doped ZnO nanoparticle; Table S2: Percent lattice composition, adsorbed, and defect oxygen for undoped and doped ZnO nanoparticles [19,59–63].

Author Contributions: A.W.M. and J.Z. developed the project and designed the experiments. A.W.M. carried out all the syntheses, photocatalytic measurements, diffuse reflectance spectroscopy analyses, and XRD characterization under the guidance of J.Z. and C.S. performed the SEM analysis. T.K.T.T. carried out the TEM characterization. H.N.N. assisted in some of the optical measurements. X.H., T.S.B. and R.B. prepared the samples and measured and analyzed the photocurrent density data under the guidance of S.L.S. and A.D.A. measured and analyzed the XPS data under the guidance of S.L.S. All authors contributed to the writing of the manuscript. All authors have read and agreed to the published version of the manuscript.

Funding: This research received no external funding.

Data Availability Statement: Data are contained within the article and supplementary materials.

Acknowledgments: J.Z. acknowledges the partial financial support from the UCONN Scholarship Facilitation Fund for this work.

Conflicts of Interest: The authors declare no conflicts of interest.

References

1. Yang, X.; Wu, J.; Qi, Y.; Liu, S.; Hosseini-Bandegharai, A.; Zhong, Y.; Liu, X.; Chen, Q.; Yu, J. Progress and Outlook of Surface Engineering Strategies in Photocatalytic Materials for Mercury Removal: A Review. *Energy Fuels* **2023**, *37*, 13579–13600. [[CrossRef](#)]
2. Low, J.; Yu, J.; Jaroniec, M.; Wageh, S.; Al-Ghamdi, A.A. Heterojunction Photocatalysts. *Adv. Mater.* **2017**, *29*, 1601694. [[CrossRef](#)] [[PubMed](#)]
3. Di Liberto, G.; Cipriano, L.A.; Tosoni, S.; Pacchioni, G. Rational Design of Semiconductor Heterojunctions for Photocatalysis. *Chem. Eur. J.* **2021**, *27*, 13306–13317. [[CrossRef](#)] [[PubMed](#)]
4. Kosco, J.; Gonzalez-Carrero, S.; Howells, C.T.; Fei, T.; Dong, Y.; Sougrat, R.; Harrison, G.T.; Firdaus, Y.; Sheelamantula, R.; Purushothaman, B.; et al. Generation of Long-Lived Charges in Organic Semiconductor Heterojunction Nanoparticles for Efficient Photocatalytic Hydrogen Evolution. *Nat. Energy* **2022**, *7*, 340–351. [[CrossRef](#)]
5. Yang, Y.; Liu, B.; Xu, J.; Wang, Q.; Wang, X.; Lv, G.; Zhou, J. The Synthesis of H-BN-Modified Z-Scheme $\text{WO}_3/\text{g-C}_3\text{N}_4$ Heterojunctions for Enhancing Visible Light Photocatalytic Degradation of Tetracycline Pollutants. *ACS Omega* **2022**, *7*, 6035–6045. [[CrossRef](#)] [[PubMed](#)]
6. Wang, Z.; Ning, X.; Feng, Y.; Zhang, R.; He, Y.; Zhao, H.; Chen, J.; Du, P.; Lu, X. Insights into the Enhanced Photoelectrochemical Performance through Construction of the Z-Scheme and Type II Heterojunctions. *Anal. Chem.* **2022**, *94*, 8539–8546. [[CrossRef](#)] [[PubMed](#)]
7. Wang, H.; Zhang, L.; Chen, Z.; Hu, J.; Li, S.; Wang, Z.; Liu, J.; Wang, X. Semiconductor Heterojunction Photocatalysts: Design, Construction, and Photocatalytic Performances. *Chem. Soc. Rev.* **2014**, *43*, 5234–5244. [[CrossRef](#)] [[PubMed](#)]
8. Di, T.; Xu, Q.; Ho, W.; Tang, H.; Xiang, Q.; Yu, J. Review on Metal Sulphide-based Z-scheme Photocatalysts. *ChemCatChem* **2019**, *11*, 1394–1411. [[CrossRef](#)]

9. Zhao, W.; Feng, Y.; Huang, H.; Zhou, P.; Li, J.; Zhang, L.; Dai, B.; Xu, J.; Zhu, F.; Sheng, N.; et al. A Novel Z-Scheme $\text{Ag}_3\text{VO}_4/\text{BiVO}_4$ Heterojunction Photocatalyst: Study on the Excellent Photocatalytic Performance and Photocatalytic Mechanism. *Appl. Catal. B Environ.* **2019**, *245*, 448–458. [[CrossRef](#)]
10. Liu, X.; Zhang, Q.; Ma, D. Advances in 2D/2D Z-Scheme Heterojunctions for Photocatalytic Applications. *Sol. RRL* **2021**, *5*, 2000397. [[CrossRef](#)]
11. Lai, Y.-J.; Lee, D.-J. Pollutant Degradation with Mediator Z-Scheme Heterojunction Photocatalyst in Water: A Review. *Chemosphere* **2021**, *282*, 131059. [[CrossRef](#)] [[PubMed](#)]
12. Su, Q.; Li, Y.; Hu, R.; Song, F.; Liu, S.; Guo, C.; Zhu, S.; Liu, W.; Pan, J. Heterojunction Photocatalysts Based on 2D Materials: The Role of Configuration. *Adv. Sustain. Syst.* **2020**, *4*, 2000130. [[CrossRef](#)]
13. Liu, G.; Chen, J.; Xie, Z.; Lin, S.; Xie, L.; Deng, Y.; Lu, C.-Z. Hydrothermal Synthesis of $\text{Cd}_{0.5}\text{Zn}_{0.5}\text{S}/\text{ZnO}$ Heterojunctions with Controlled pH and Enhanced Photocatalytic Hydrogen Production Activity. *ACS Appl. Energy Mater.* **2022**, *5*, 3502–3513. [[CrossRef](#)]
14. Low, J.; Jiang, C.; Cheng, B.; Wageh, S.; Al-Ghamdi, A.A.; Yu, J. A Review of Direct Z-Scheme Photocatalysts. *Small Methods* **2017**, *1*, 1700080. [[CrossRef](#)]
15. Bohle, D.S.; Spina, C.J. Cationic and Anionic Surface Binding Sites on Nanocrystalline Zinc Oxide: Surface Influence on Photoluminescence and Photocatalysis. *J. Am. Chem. Soc.* **2009**, *131*, 4397–4404. [[CrossRef](#)] [[PubMed](#)]
16. Luo, L.; Gong, Z.; Xu, Y.; Ma, J.; Liu, H.; Xing, J.; Tang, J. Binary Au–Cu Reaction Sites Decorated ZnO for Selective Methane Oxidation to C1 Oxygenates with Nearly 100% Selectivity at Room Temperature. *J. Am. Chem. Soc.* **2022**, *144*, 740–750. [[CrossRef](#)] [[PubMed](#)]
17. Pradeev Raj, K.; Sadaiyandi, K.; Kennedy, A.; Sagadevan, S.; Chowdhury, Z.Z.; Johan, M.R.B.; Aziz, F.A.; Rafique, R.F.; Thamiz Selvi, R.; Rathina Bala, R. Influence of Mg Doping on ZnO Nanoparticles for Enhanced Photocatalytic Evaluation and Antibacterial Analysis. *Nanoscale Res. Lett.* **2018**, *13*, 229. [[CrossRef](#)]
18. Macías-Sánchez, J.J.; Hinojosa-Reyes, L.; Caballero-Quintero, A.; De La Cruz, W.; Ruiz-Ruiz, E.; Hernández-Ramírez, A.; Guzmán-Mar, J.L. Synthesis of Nitrogen-Doped ZnO by Sol–Gel Method: Characterization and Its Application on Visible Photocatalytic Degradation of 2,4-D and Picloram Herbicides. *Photochem. Photobiol. Sci.* **2015**, *14*, 536–542. [[CrossRef](#)]
19. Hailili, R.; Ji, H.; Wang, K.; Dong, X.; Chen, C.; Sheng, H.; Bahnemann, D.W.; Zhao, J. ZnO with Controllable Oxygen Vacancies for Photocatalytic Nitrogen Oxide Removal. *ACS Catal.* **2022**, *12*, 10004–10017. [[CrossRef](#)]
20. Liu, B.; Bie, C.; Zhang, Y.; Wang, L.; Li, Y.; Yu, J. Hierarchically Porous ZnO/g- C_3N_4 S-Scheme Heterojunction Photocatalyst for Efficient H_2O_2 Production. *Langmuir* **2021**, *37*, 14114–14124. [[CrossRef](#)]
21. Li, X.; Chen, Y.; Tao, Y.; Shen, L.; Xu, Z.; Bian, Z.; Li, H. Challenges of Photocatalysis and Their Coping Strategies. *Chem. Catal.* **2022**, *2*, 1315–1345. [[CrossRef](#)]
22. Xu, Z.; Zheng, R.; Chen, Y.; Zhu, J.; Bian, Z. Ordered Mesoporous Fe/TiO₂ with Light Enhanced Photo-Fenton Activity. *Chin. J. Catal.* **2019**, *40*, 631–637. [[CrossRef](#)]
23. Du, H.; Liang, K.; Yuan, C.-Z.; Guo, H.-L.; Zhou, X.; Jiang, Y.-F.; Xu, A.-W. Bare $\text{Cd}_{1-x}\text{Zn}_x\text{S}$ ZB/WZ Heterophase Nanojunctions for Visible Light Photocatalytic Hydrogen Production with High Efficiency. *ACS Appl. Mater. Interfaces* **2016**, *8*, 24550–24558. [[CrossRef](#)] [[PubMed](#)]
24. Priyanka; Srivastava, V.C. Photocatalytic Oxidation of Dye Bearing Wastewater by Iron Doped Zinc Oxide. *Ind. Eng. Chem. Res.* **2013**, *52*, 17790–17799. [[CrossRef](#)]
25. Achouri, F.; Corbel, S.; Balan, L.; Mozet, K.; Giro, E.; Medjahdi, G.; Said, M.B.; Ghrabi, A.; Schneider, R. Porous Mn-Doped ZnO Nanoparticles for Enhanced Solar and Visible Light Photocatalysis. *Mater. Des.* **2016**, *101*, 309–316. [[CrossRef](#)]
26. Samadi, M.; Zirak, M.; Naseri, A.; Khorashadizade, E.; Moshfegh, A.Z. Recent Progress on Doped ZnO Nanostructures for Visible-Light Photocatalysis. *Thin Solid Film.* **2016**, *605*, 2–19. [[CrossRef](#)]
27. Hafdallah, A.; Ynineb, F.; Aida, M.S.; Attaf, N. In Doped ZnO Thin Films. *J. Alloys Compd.* **2011**, *509*, 7267–7270. [[CrossRef](#)]
28. Musat, V.; Teixeira, B.; Fortunato, E.; Monteiro, R.C.C.; Vilarinho, P. Al-Doped ZnO Thin Films by Sol–Gel Method. *Surf. Coat. Technol.* **2004**, *180–181*, 659–662. [[CrossRef](#)]
29. Faraz, M.; Naqvi, F.K.; Shakir, M.; Khare, N. Synthesis of Samarium-Doped Zinc Oxide Nanoparticles with Improved Photocatalytic Performance and Recyclability under Visible Light Irradiation. *New J. Chem.* **2018**, *42*, 2295–2305. [[CrossRef](#)]
30. Pan, H.; Yi, J.B.; Shen, L.; Wu, R.Q.; Yang, J.H.; Lin, J.Y.; Feng, Y.P.; Ding, J.; Van, L.H.; Yin, J.H. Room-Temperature Ferromagnetism in Carbon-Doped ZnO. *Phys. Rev. Lett.* **2007**, *99*, 127201. [[CrossRef](#)]
31. Kulkarni, D.R.; Malode, S.J.; Keerthi Prabhu, K.; Ayachit, N.H.; Kulkarni, R.M.; Shetti, N.P. Development of a Novel Nanosensor Using Ca-Doped ZnO for Antihistamine Drug. *Mater. Chem. Phys.* **2020**, *246*, 122791. [[CrossRef](#)]
32. Jun, M.-C.; Park, S.-U.; Koh, J.-H. Comparative Studies of Al-Doped ZnO and Ga-Doped ZnO Transparent Conducting Oxide Thin Films. *Nanoscale Res. Lett.* **2012**, *7*, 639. [[CrossRef](#)] [[PubMed](#)]
33. Ji, Z.; Luo, Z.; Li, J.; Li, P. Enhanced Photocatalytic Activity of ZnO Toward the Degradation of Methylene Blue Dye: Effects of Fe^{3+} and Sn^{4+} Doping. *Phys. Status Solidi A* **2019**, *216*, 1800947. [[CrossRef](#)]
34. Kazunori Sato, K.S.; Hiroshi Katayama-Yoshida, H.K.-Y. Stabilization of Ferromagnetic States by Electron Doping in Fe-, Co- or Ni-Doped ZnO. *Jpn. J. Appl. Phys.* **2001**, *40*, L334. [[CrossRef](#)]
35. Van Embden, J.; Gross, S.; Kittilstved, K.R.; Della Gaspera, E. Colloidal Approaches to Zinc Oxide Nanocrystals. *Chem. Rev.* **2023**, *123*, 271–326. [[CrossRef](#)] [[PubMed](#)]

36. Qamar, M.A.; Javed, M.; Shahid, S.; Sher, M. Fabrication of G-C₃N₄/Transition Metal (Fe, Co, Ni, Mn and Cr)-Doped ZnO Ternary Composites: Excellent Visible Light Active Photocatalysts for the Degradation of Organic Pollutants from Wastewater. *Mater. Res. Bull.* **2022**, *147*, 111630. [[CrossRef](#)]
37. Karunakaran, C.; Vijayabalan, A.; Manikandan, G. Photocatalytic and Bactericidal Activities of Hydrothermally Synthesized Nanocrystalline Cd-Doped ZnO. *Superlattices Microstruct.* **2012**, *51*, 443–453. [[CrossRef](#)]
38. Ahn, B.D.; Kang, H.S.; Kim, J.H.; Kim, G.H. Synthesis and Analysis of Ag-Doped ZnO. *J. Appl. Phys.* **2006**, *100*, 093701. [[CrossRef](#)]
39. Hongsith, N.; Viriyaworasakul, C.; Mangkorntong, P.; Mangkorntong, N.; Chooapun, S. Ethanol Sensor Based on ZnO and Au-Doped ZnO Nanowires. *Ceram. Int.* **2008**, *34*, 823–826. [[CrossRef](#)]
40. Liu, Y.; Zhang, Q.; Xu, M.; Yuan, H.; Chen, Y.; Zhang, J.; Luo, K.; Zhang, J.; You, B. Novel and Efficient Synthesis of Ag-ZnO Nanoparticles for the Sunlight-Induced Photocatalytic Degradation. *Appl. Surf. Sci.* **2019**, *476*, 632–640. [[CrossRef](#)]
41. Tabassum, L.; Tasnim, H.; Meguerdichian, A.G.; Willis, W.S.; Macharia, J.; Price, C.; Dang, Y.; Suib, S.L. Enhanced Catalytic Activity of a Vanadium-Doped Mesoporous Octahedral Molecular Sieve-2 (K-OMS-2) toward Hydrogen Evolution Reaction. *ACS Appl. Energy Mater.* **2020**, *3*, 12185–12193. [[CrossRef](#)]
42. Nair, M.G.; Nirmala, M.; Rekha, K.; Anukaliani, A. Structural, Optical, Photo Catalytic and Antibacterial Activity of ZnO and Co Doped ZnO Nanoparticles. *Mater. Lett.* **2011**, *65*, 1797–1800. [[CrossRef](#)]
43. Adeel, M.; Saeed, M.; Khan, I.; Muneer, M.; Akram, N. Synthesis and Characterization of Co-ZnO and Evaluation of Its Photocatalytic Activity for Photodegradation of Methyl Orange. *ACS Omega* **2021**, *6*, 1426–1435. [[CrossRef](#)] [[PubMed](#)]
44. Zeferino, R.S.; Flores, M.B.; Pal, U. Photoluminescence and Raman Scattering in Ag-Doped ZnO Nanoparticles. *J. Appl. Phys.* **2011**, *109*, 014308. [[CrossRef](#)]
45. Yang, J.; Gao, M.; Yang, L.; Zhang, Y.; Lang, J.; Wang, D.; Wang, Y.; Liu, H.; Fan, H. Low-Temperature Growth and Optical Properties of Ce-Doped ZnO Nanorods. *Appl. Surf. Sci.* **2008**, *255*, 2646–2650. [[CrossRef](#)]
46. Wagh, S.S.; Kadam, V.S.; Jagtap, C.V.; Salunkhe, D.B.; Patil, R.S.; Pathan, H.M.; Patole, S.P. Comparative Studies on Synthesis, Characterization and Photocatalytic Activity of Ag Doped ZnO Nanoparticles. *ACS Omega* **2023**, *8*, 7779–7790. [[CrossRef](#)] [[PubMed](#)]
47. Chitradevi, T.; Jestin Lenus, A.; Victor Jaya, N. Structure, Morphology and Luminescence Properties of Sol-Gel Method Synthesized Pure and Ag-Doped ZnO Nanoparticles. *Mater. Res. Express* **2020**, *7*, 015011. [[CrossRef](#)]
48. Yusuf, T.L.; Orimolade, B.O.; Masekela, D.; Mamba, B.; Mabuba, N. The Application of Photoelectrocatalysis in the Degradation of Rhodamine B in Aqueous Solutions: A Review. *RSC Adv.* **2022**, *12*, 26176–26191. [[CrossRef](#)]
49. Kenchappa Somashekharappa, K.; Lokesh, S.V. Hydrothermal Synthesis of K₂Ti₆O₁₃ Nanotubes/Nanoparticles: A Photodegradation Study on Methylene Blue and Rhodamine B Dyes. *ACS Omega* **2021**, *6*, 7248–7256. [[CrossRef](#)]
50. Lee, Y.Y.; Moon, J.H.; Choi, Y.S.; Park, G.O.; Jin, M.; Jin, L.Y.; Li, D.; Lee, J.Y.; Son, S.U.; Kim, J.M. Visible-Light Driven Photocatalytic Degradation of Organic Dyes over Ordered Mesoporous Cd_xZn_{1-x}S Materials. *J. Phys. Chem. C* **2017**, *121*, 5137–5144. [[CrossRef](#)]
51. Nabi, G.; Malik, N.; Tahir, M.B.; Tanveer, M.; Rafique, R.; Rehman, S.; Yousaf, R.; Akram, S. Synthesis of G-C₃N₄ Nanorods for Visible-Light Photocatalytic Degradation of Methylene Blue, Methylene Orange and Rhodamine-B. *Int. J. Environ. Anal. Chem.* **2022**, *102*, 8503–8518. [[CrossRef](#)]
52. Utami, M.; Wang, S.; Fajarwati, F.I.; Salsabilla, S.N.; Dewi, T.A.; Fitri, M. Enhanced Photodegradation of Rhodamine B Using Visible-Light Sensitive N-TiO₂/rGO Composite. *Crystals* **2023**, *13*, 588. [[CrossRef](#)]
53. Ahmad, I. Comparative Study of Metal (Al, Mg, Ni, Cu and Ag) Doped ZnO/g-C₃N₄ Composites: Efficient Photocatalysts for the Degradation of Organic Pollutants. *Sep. Purif. Technol.* **2020**, *251*, 117372. [[CrossRef](#)]
54. Feng, J.; Zhang, D.; Zhou, H.; Pi, M.; Wang, X.; Chen, S. Coupling P Nanostructures with P-Doped g-C₃N₄ As Efficient Visible Light Photocatalysts for H₂ Evolution and RhB Degradation. *ACS Sustain. Chem. Eng.* **2018**, *6*, 6342–6349. [[CrossRef](#)]
55. Firet, N.J.; Blommaert, M.A.; Burdyny, T.; Venugopal, A.; Bohra, D.; Longo, A.; Smith, W.A. Operando EXAFS Study Reveals Presence of Oxygen in Oxide-Derived Silver Catalysts for Electrochemical CO₂ Reduction. *J. Mater. Chem. A* **2019**, *7*, 2597–2607. [[CrossRef](#)]
56. Wang, Y.; Nyiera, H.N.; Mureithi, A.W.; Sun, Y.; Mani, T.; Zhao, J. Length-Dependent Photocatalytic Activity of Hybrid Ag-CdS Nanorods. *J. Phys. Chem. C* **2022**, *126*, 15685–15693. [[CrossRef](#)]
57. Rabell, G.O.; Cruz, M.R.A.; Juárez-Ramírez, I. Hydrogen Production of ZnO and ZnO/Ag Films by Photocatalysis and Photoelectrocatalysis. *Mater. Sci. Semicond. Process.* **2021**, *134*, 105985. [[CrossRef](#)]
58. Sreedhar, A.; Reddy, I.N.; Hoai Ta, Q.T.; Namgung, G.; Cho, E.; Noh, J.-S. Facile Growth of Novel Morphology Correlated Ag/Co-Doped ZnO Nanowire/Flake-like Composites for Superior Photoelectrochemical Water Splitting Activity. *Ceram. Int.* **2019**, *45*, 6985–6993. [[CrossRef](#)]
59. Zhou, G.; Meng, L.; Ning, X.; Yin, W.; Hou, J.; Xu, Q.; Yi, J.; Wang, S.; Wang, X. Switching Charge Transfer of G-C₃N₄/BiVO₄ Heterojunction from Type II to Z-Scheme via Interfacial Vacancy Engineering for Improved Photocatalysis. *Int. J. Hydrogen Energy* **2022**, *47*, 8749–8760. [[CrossRef](#)]
60. Ma, Z.; Ren, F.; Ming, X.; Long, Y.; Volinsky, A.A. Cu-Doped ZnO Electronic Structure and Optical Properties Studied by First-Principles Calculations and Experiments. *Materials* **2019**, *12*, 196. [[CrossRef](#)]
61. Qamar, M.A.; Javed, M.; Shahid, S.; Iqbal, S.; Abubshait, S.A.; Abubshait, H.A.; Ramay, S.M.; Mahmood, A.; Ghaitan, H.M. Designing of Highly Active G-C₃N₄/Co@ZnO Ternary Nanocomposites for the Disinfection of Pathogens and Degradation of the Organic Pollutants from Wastewater under Visible Light. *J. Environ. Chem. Eng.* **2021**, *9*, 105534. [[CrossRef](#)]

62. Feng, N.; Wang, Q.; Zheng, A.; Zhang, Z.; Fan, J.; Liu, S.-B.; Amoureux, J.-P.; Deng, F. Understanding the High Photocatalytic Activity of (B, Ag)-Codoped TiO₂ under Solar-Light Irradiation with XPS, Solid-State NMR, and DFT Calculations. *J. Am. Chem. Soc.* **2013**, *135*, 1607–1616. [[CrossRef](#)] [[PubMed](#)]
63. Nguyen, S.N.; Truong, T.K.; You, S.-J.; Wang, Y.-F.; Cao, T.M.; Pham, V.V. Investigation on Photocatalytic Removal of NO under Visible Light over Cr-Doped ZnO Nanoparticles. *ACS Omega* **2019**, *4*, 12853–12859. [[CrossRef](#)] [[PubMed](#)]

Disclaimer/Publisher's Note: The statements, opinions and data contained in all publications are solely those of the individual author(s) and contributor(s) and not of MDPI and/or the editor(s). MDPI and/or the editor(s) disclaim responsibility for any injury to people or property resulting from any ideas, methods, instructions or products referred to in the content.